

Multiscale prediction of microstructure length scales in metallic alloy casting

B. Bellon^{1,2}, A.K. Boukellal¹, T. Isensee^{1,2}, O.M. Wellborn³, K.P. Trumble³, M.J.M. Krane³, M.S. Titus³,
D. Tourret¹, J. LLorca^{1,2*}

¹ *IMDEA Materials Institute, C/ Eric Kandel 2, 28906, Getafe, Madrid, Spain.*

² *Department of Materials Science, Polytechnic University of Madrid/Universidad Politécnic de Madrid, E.T.S. de Ingenieros de Caminos. 28040 - Madrid, Spain.*

³ *Purdue Center for Metal Casting Research, School of Materials Engineering, Purdue University, West Lafayette, Indiana, USA.*

Abstract

Microstructural length scales, such as dendritic spacings in cast metallic alloys, play an essential role in the properties of structural components. Therefore, quantitative prediction of such length scales through simulations is important to design novel alloys and optimize processing conditions through integrated computational materials engineering (ICME). Thus far, quantitative comparisons between experiments and simulations of primary dendrite arms spacings (PDAS) selection in metallic alloys have been mainly limited to directional solidification of thin samples and quantitative phase-field simulations of dilute alloys. In this article, we combine casting experiments and quantitative simulations to present a novel multiscale modeling approach to predict local primary dendritic spacings in metallic alloys solidified in conditions relevant to industrial casting processes. To this end, primary dendritic spacings were measured in instrumented casting experiments in Al-Cu alloys containing 1 wt% and 4 wt% of Cu, and they were compared to spacing stability ranges and average spacings in dendritic arrays simulated using phase-field (PF) and dendritic needle network (DNN) models. It is first shown that PF and DNN lead to similar results for the Al-1 wt%Cu alloy, using a dendrite tip selection constant calculated with PF in the DNN simulations. PF simulations cannot achieve quantitative predictions for the Al-4 wt%Cu alloy because they are too computationally demanding due to the large separation of scale between tip radius and diffusion length, a characteristic feature of non-dilute alloys. Nevertheless, the results of DNN simulations for non-dilute Al-Cu alloys are in overall good agreement with our experimental results as well as with those of an extensive literature review. Simulations consistently suggest a widening of the PDAS stability range with a decrease of the temperature gradient as the microstructure goes from cellular-dendrites to well-developed hierarchical dendrites.

Keywords: Solidification, Casting, Metallic alloy, Microstructure, Multiscale modeling.

1. Introduction

Solidification is the initial processing step for most metallic alloys. Microstructural features that develop during solidification play a key role in the properties, performance and lifetime of cast metal parts. Even when the microstructure later evolves through additional complex thermomechanical pro-

cessing steps, the starting point is the microstructure that emerges from the liquid state. Dendrites, which are branched structures with primary, secondary and higher-order branches, are among the most common microstructural features in cast alloys [1–3]. Dendritic microstructures exhibit several important characteristic length scales, such as dendrite tip radius or dendrite arm spacings. These spacings directly affect the mechanical properties of individual grains [1, 2], in particular ultimate tensile strength and yield strength (see, e.g., [4–6]).

*Corresponding author; Email address: javier.llorca@imdea.org

They also set the scale for solute (micro)segregation [1, 2, 7], which has a strong effect on the potential appearance of defects (e.g. freckles) or secondary phases (e.g. precipitates or eutectics), as well as on electrochemical properties, such as corrosion resistance (see, e.g., [6, 8, 9]). Primary dendrite arm spacings (PDAS) also play a key role in the permeability of semi-solid microstructures [10–14], which has major influence on the appearance of critical defects, such as hot tears.

During growth of primary dendrites, the selection of dendrite tip radius ρ is unique for a given set of solidification conditions (namely, solute concentration c_∞ , solidification velocity V , and thermal gradient G) and follows the microscopic solvability theory [15–19].

The selection of PDAS, on the other hand, is not unique. A given set of parameters may yield a wide distribution of spacings [20–26], even though a similar processing history tends to lead to narrowly distributed spacings [26, 27]. Over the years, many studies have focused on the link between the solidification conditions and the morphological characteristics of dendrites (see e.g. [22, 26, 28, 29] among others). Most models for the PDAS rely on phenomenological relations linking the primary spacing λ to processing parameters in the form of power laws such as [28]:

$$\lambda = KG^{-a}V^{-b} \quad (1)$$

where the exponent a is often close to 0.5, b typically varies between 0.25 and 0.5, and K is a prefactor that depends on alloy parameters, such as its composition and phase diagram features (e.g. solute partition coefficient) [22, 26, 29, 30]. However, experimental evidence indicates that a wide range of PDAS can be obtained under similar solidification conditions. The lower limit of the PDAS stability range, λ_{min} , is linked to an elimination instability [26, 31–34], while the upper stability limit, λ_{max} , stems from a branching instability. The determination of this range is not, however, trivial considering all the mechanisms involved, including: tip elimination through thermal and solutal interaction, tip splitting, secondary and tertiary arm development, lateral migration, thermo-solutal convection, and defect interaction with the growth front.

Directional solidification is the standard experimental approach to establish the link between solidification conditions and microstructure in metallic alloys. Particularly, dendrite growth in the Al-Cu system has been studied for many solidification

conditions (G and V), different Cu concentrations and different experimental set-ups. They include standard Bridgman furnaces in which the solidification velocity is controlled [35–38], or small volumes in which solidification takes place under a given thermal gradient [39–43], while other studies used larger molds in which the temperature was measured along the solidification direction to obtain the thermal gradient and the solidification velocity [44–47]. The differences in solidification conditions has led to a significant scatter in the PDAS for similar nominal values of the solidification process, as given by the cooling rate $R = GV$, but the overall trend is clearly indicative of the power law behavior from phenomenological scaling laws (see Fig. I of the Supplementary Material).

Further analysis of the parameters controlling microstructural development during solidification can be obtained through modeling and simulation.

Conventional models for macroscopic solidification processes (e.g. casting) rely on conservation equations averaged over multi-phase domains, such that a field corresponding to the average fraction of phase over representative volume elements appears in the equations [48–54]. The fraction of phases may be tabulated as a function of temperature using classical solidification paths such as lever rule or Gulliver-Scheil model [29]. Alternatively, microstructural length scales (e.g. dendritic spacings) may be introduced in the equations to model the kinetics of solute microsegregation between dendritic branches a bit more accurately [50–56]. These length scales are then typically estimated from phenomenological power laws such as Eq. (1).

Models capable of estimating microstructural length scales require a relatively more precise spatial description, consistent with the scale of the features one aims at predicting. This makes simulations computationally challenging since they have to combine phenomena across a wide range of scales, from microscopic capillarity at dendritic tips to macroscopic transport of heat and solute in the melt. Simulations of dendritic spacings have been performed with a range of models based on cellular automata (CA) [57–59], grain envelopes [60, 61], dendritic needle networks (DNN) [62–65] and phase fields (PF) [66–68]. Approximate — and computationally efficient — models (e.g. CA) rely on stringent assumptions and phenomenological laws, for instance directly relating the growth kinetics of dendrite tips to some measure of the local driving force for solidification (e.g. undercooling or solute

supersaturation measured at a given distance from the solid-liquid interface). The most accurate models (e.g. PF) rely solely on fundamental concepts of diffuse interface thermodynamics [69, 70] and allow quantitative calculations directly from thermophysical alloy parameters and processing conditions. However, they remain limited in length and time scales by their relatively high computational cost. Hence, a multiscale multi-model bottom-up strategy appears to be a promising route to address the limitations of each models.

Here we specifically focus on two modeling methods, namely PF and DNN, and we show that quantitative PF simulations of dendritic growth in dilute alloys can be quantitatively upscaled and expanded to non-dilute compositions using the multiscale DNN approach.

The PF method is now recognized as the outstanding tool to predict microstructural patterns resulting from nonequilibrium solidification [69–71]. The method allows modeling the evolution of solid-liquid interfaces and complex microstructural patterns, such as dendrites. It has been applied to the solidification of Al-Cu alloys, at first qualitatively, e.g. to reproduce scaling laws for secondary dendrite arm spacing in cast samples [72]. Then, the development of quantitative models for dilute binary alloys [73–76] has allowed direct quantitative comparisons with directional solidification experiments of dilute Al-Cu thin-samples imaged in situ with X-ray radiography [68]. However, quantitative PF predictions are still constrained by the requirement of an accurate description of the local solid-liquid interface curvature. This limits the size of the grid elements required in the vicinity of each dendritic tip for primary, secondary, and higher-order side-branches. This limitation may, to some extent, be addressed through parallelization [77, 78] and advanced numerics (e.g. adaptive meshing [79–81] or implicit time stepping [82, 83]). However, quantitative PF simulations become challenging, if feasible at all, beyond the dilute alloy limit, as the separation of scale between interfacial capillary length, dendrite tip radius, and solute transport in the bulk becomes extreme.

In order to overcome this limitation, the dendritic needle network (DNN) method was developed to bridge the scale of the microscopic dendrite tip radius, ρ , and that of solute transport in the liquid phase, e.g. the diffusion length $l_D = D/V$ with D the solute diffusivity. The DNN model represents a dendritic crystal as a network of parabolic-shaped

needles, that approximate the primary stems and higher order branches. The DNN model combines the microscopic solvability theory established at the scale of the tip radius [15–18] with a solute mass balance established at the “mesoscale” between ρ and l_D , to calculate the instantaneous growth velocities of individual dendrite tips [62, 63, 84, 85]. The numerical spatial discretization can be taken at the same order as the tip radius, such that the domain size can be considerably larger than in equivalent PF simulation, in particular for concentrated alloys with $\rho \ll l_D$. DNN simulations have been verified to reproduce analytical and phase-field predictions for steady-state and transient growth kinetics [62, 63, 86]. First DNN applications to the prediction of primary dendritic spacings in binary Al alloys, compared to well-controlled thin-sample directional solidification experiments [63, 87, 88], have shown promising results.

This investigation is aimed at bridging length scales in the simulation of alloy solidification. One central objective is to demonstrate that microstructural length scales, such as PDAS, can be computationally predicted for a bulk specimen, under conditions distinctive from a Bridgman type experiment, namely nonuniform G , V and non-negligible fluid flow, making it closer and thus more representative of solidification conditions for industrial casting processing. To do so, we performed casting experiments of binary Al-Cu alloys, and combined simulations at distinct length scales. First, we show that both PF and DNN can provide reliable predictions of stability range of PDAS for an Al-1 wt%Cu alloy. Then, we use the computationally-efficient DNN model to calculate the PDAS stability range for a more concentrated Al-4 wt%Cu alloy. We discuss and compare our results with a broad range of experimental literature data for Al-Cu alloys. Overall, the article shows how multiscale modeling can provide quantitative predictions of important microstructural features (e.g. PDAS) during solidification of non-dilute alloys at experimentally relevant length and time scales using physics-based computational models.

2. Methods

Here, we provide a short description of our experimental and computational methods. A more thorough description with full details of equipments, procedures, equations, and algorithms is provided in the joint Supplementary Material document.

2.1. Experiments and characterization

2.1.1. Casting experiments

We performed casting experiments in the facilities of the School of Materials Engineering at Purdue University. Two different Al-Cu alloys with 1 and 4 wt%Cu were prepared by melting Al granules and Cu rods in a clay-graphite crucible using an air induction furnace. The alloys were poured into a stainless steel mold, of dimensions shown in Fig. 1a. The mold assembly was wrapped with a heating tape to reach approximately 500°C before pouring. Prior to pouring through the riser, the heating tape was disconnected. The exterior of the mold was covered with several layers of an insulating blanket to minimize the heat losses through the mold walls.

The heat was extracted from the side of the mold by a water-cooled chill plate (Fig. 1b), promoting predominantly horizontal directional solidification. For each alloy, we explored different cooling rates by performing two sets of experiments: either (1) with a 0.2 mm thick copper shim between the chill plate and the mold, thus ensuring good thermal contact, or (2) with an additional 5 mm thick alumina plate between the chill plate and the copper shim, thus reducing the heat extraction rate. The mold was

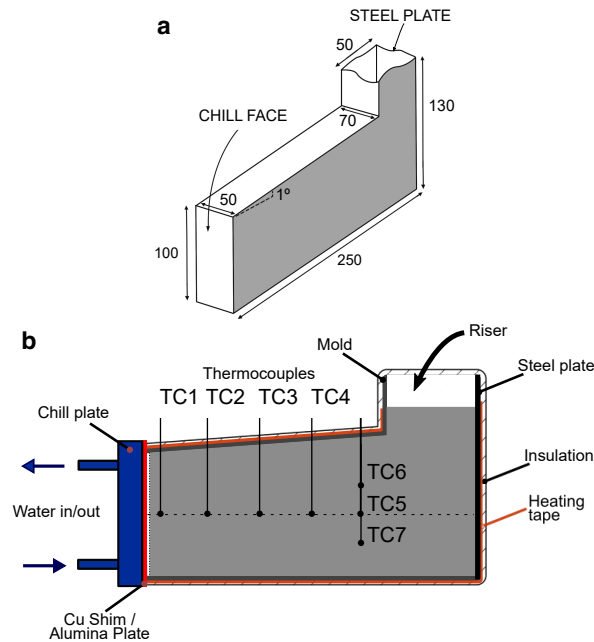


Figure 1: Experimental setup for casting experiments: (a) Schematics and dimensions (in mm) of the mold; (b) Mold assembly schematics (not to scale) showing the locations of thermocouples TC1 through TC7.

instrumented with 7 K-type thermocouples, shown in Fig. 1b (also see Table I of the Supplementary Material), mechanically joined and protected from dissolution by high-temperature cement.

2.1.2. Microstructure characterization

We sectioned the cast ingot in between the locations of thermocouples and cut out cross-sections of about $30 \times 30 \text{ mm}^2$. Their surface was polished using SiC paper up to 4000 grit, followed by diamond pastes down to $0.25 \mu\text{m}$ particle size, and finishing with a solution of colloidal silica (OP-S).

The polished samples were etched with Kellers reagent and observed under two different optical microscopes with magnification from $6.3 \times$ to $1000 \times$. We used the software ImageJ to enhance the image contrast and manually located the apparent centers of dendrites, measuring at least 400 primary dendrites in each specimen. The average PDAS was calculated from these locations using a standard Delaunay triangulation Python code.

We performed electron backscatter diffraction (EBSD) on the cross-sections in order to assess the misorientation between the typical [100] growth direction of Al dendrites and the cutting/observation plane. Several EBSD scans were combined into grain orientation maps in areas of about $16 \times 4 \text{ mm}^2$ and analyzed using the MTEX toolbox [89].

2.1.3. Estimation of local solidification conditions

In this article we focus primarily on the columnar dendritic structures observed between the locations of thermocouples TC1 and TC2, i.e. in the early stage of the experiment when the solidification direction is still expected to be aligned with the (horizontal) main heat extraction direction.

We estimated the velocity of isotherms between TC1 and TC2 by dividing the distance between the thermocouples by the times t_1 and t_2 at which the temperatures from TC1 and TC2 reach a given temperature T_L^- chosen up to 20 K below the alloy liquidus temperature T_L (see Section 3.1 and Fig. 3).

The local temperature gradient was estimated as an average cooling rate R of the temperatures recorded by TC1 and TC2 between times t_1 and t_2 . Practically, we performed a linear fit of TC1 and TC2 in that time range to extract their respective cooling rates R_1 and R_2 , and then considered that $R \approx (R_1 + R_2)/2$ to calculate $G = R/V$.

Since the estimation of the local velocity of isotherms V was more accurate than that of the

temperature gradient G (see section 3.1), we decided to use V as a fixed input value in both PF and DNN simulations, and to explore different values of G , i.e. different cooling rates $R = GV$.

2.2. Modeling and simulations

We used two models already described and used in several previous publications. Therefore, we only give a brief description of the models and the main simulations procedures. Nevertheless, a complete description of model equations, algorithms, and an exhaustive list numerical and alloy parameters, together with a brief discussion of the latter, are provided in the joint Supplementary Material.

2.2.1. Phase-field

We used a quantitative three-dimensional (3D) PF model for the directional solidification of a dilute binary alloy in a temperature gradient [73–76] to calculate, in conditions representative of our experiments: (1) the limits of the PDAS stability range λ_{min} and λ_{max} , (2) the dynamically selected spacing in a spatially extended array with several primary dendrites, and (3) the dendrite tip selection parameter σ . All PF simulations were performed for the Al-1 wt%Cu experiment using one growth velocity $V = 160 \mu\text{m/s}$, estimated in the experiment with the insulating alumina plate (see Section 3.1), and exploring different temperature gradients $G = 10^2, 10^3$, and 10^4 K/m

First, we calculated λ_{min} and λ_{max} in a regular quincunx (fcc-like) dendritic array, illustrated

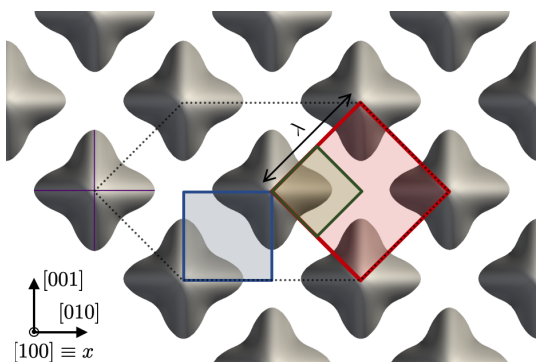


Figure 2: Simulation domains for a quincunx (fcc-like) dendritic pattern of primary spacing λ , as used in the phase-field (green and red squares) and DNN (blue square) simulations. For clarity only the tip region is shown here (up to $\approx 165 \mu\text{m}$ behind the tip) and not the region at lower temperature, in which side-branching may occur.

in Fig. 2. Thus, we simulated one quarter of a dendrite (green square in Fig. 2) with mirror symmetry imposed along all boundaries. Using a procedure already used in several previous publications [33, 90, 91] (see Supplementary Material), we progressively increased the size of the domain along y and z until a branching event occurs, thus marking the upper limit of spacing stability λ_{max} . In order to identify the lower stability limit λ_{min} , we performed simulations with four quarters of dendrites in opposite corners of the simulation box (red square in Fig. 2), and reduce the domain size until one or more primary dendrite is eliminated, thus identifying λ_{min} . Using a moving frame following the tip location in the x direction, the size of the domain in x was taken long enough for no-flux boundary conditions to have a negligible effect on the tip growth dynamics (see Supplementary Material).

Then, we performed one simulation of a spatially extended array of dendrites in a thermal gradient $G = 10^3 \text{ K/m}$, using a simulation domain of cross-section $L_y \times L_z = 512 \times 512 \mu\text{m}^2$ and length $L_x = 1185 \mu\text{m}$, starting from a planar interface located at the liquidus temperature. The simulated time was 200 s, which was found to be enough to approach an apparent steady-state microstructure.

We also used the PF results to estimate the dendrite tip selection parameter σ , which is an input parameter of the DNN model. To do so, we extracted primary tip radii in simulations of one quarter of dendrite, using least-square fitting of the solid-liquid interface in (010) and (001) planes to a second order parabola (purple lines on the left-side dendrite of Fig. 2) using the method presented in Ref. [68] (see Supplementary Material). We calculated σ for a handful of steady-state dendrites at different spacings in order to verify its independence to the PDAS in the simulations of one quarter of dendrite at $G = 10^2 \text{ K/m}$. We selected the lowest of the explored temperature gradients as it is well within the well-developed dendritic regime, i.e. far from the cell-to-dendrite transition regime.

2.2.2. Dendritic Needle Network

We used a multiscale 3D DNN model for directional solidification already presented elsewhere [62, 63, 84] in order to calculate, for both Al-1 wt%Cu and Al-4 wt%Cu alloys: (1) the PDAS stability limits λ_{min} and λ_{max} and (2) dynamically selected spacings in a spatially extended dendritic array.

For each alloy, we used one growth velocity estimated between thermocouples TC1 and TC2 in

the experiments with an insulating alumina plate, namely $V = 160 \mu\text{m/s}$ (Al-1 wt%Cu) and $V = 200 \mu\text{m/s}$ (Al-4 wt%Cu). We scanned a range of temperature gradient $G = 10^2, 10^3, \text{ and } 10^4 \text{ K/m}$ for $c_\infty = 1 \text{ wt\%Cu}$ and $G = 5 \times 10^2, 5 \times 10^3, \text{ and } 5 \times 10^4 \text{ K/m}$ for $c_\infty = 4 \text{ wt\%Cu}$. The value of the tip selection parameter, $\sigma = 0.063$, was estimated from phase-field simulation results.

To estimate both λ_{min} and λ_{max} , DNN simulations were initialized with two primary dendrites in opposite corners of the simulation domain (blue square in Fig. 2). Simulations were performed for different domain sizes $L_y = L_z = \lambda/\sqrt{2}$ in order to identify spacings leading to the elimination of one of the two primary dendrite (when $\lambda < \lambda_{min}$) or to the emergence of a tertiary branch as a new primary dendrite (when $\lambda > \lambda_{max}$). Similarly as in PF simulations, we use a moving frame in the x direction and the length of the domain in x was chosen long enough for boundary conditions to have a negligible effect (see Supplementary Material).

Additionally, we performed two simulations of spatially extended dendritic arrays to determine a dynamically selected average PDAS $\langle \lambda \rangle$. For the Al-1 wt%Cu alloy, we used $G = 10^3 \text{ K/m}$ and $V = 160 \mu\text{m/s}$ in a domain of size $L_y = L_z = 1138 \mu\text{m}$, and for the Al-4 wt%Cu alloy, we used $G = 5 \times 10^2 \text{ K/m}$ and $V = 200 \mu\text{m/s}$ in a domain of size $L_y = L_z = 692 \mu\text{m}$, both with a length $L_x = 1280 \mu\text{m}$. The domain was initialized with respectively 1849 and 576 uniformly distributed primary needles evenly spaced in y and z , in order to approximate a planar interface located at the alloy liquidus temperature. The simulated time were 200s and 100s, respectively, which was found sufficient to approach a steady microstructure with no further primary dendrite elimination.

3. Results

3.1. Casting

The temperature-time curves recorded by the 7 thermocouples are plotted in Fig. 3 for the four experiments. All curves exhibit a plateau or a notable inflection below the liquidus temperature, indicative of the release of latent heat (recalescence) during solidification.

Readings from thermocouples close to the cooling surface (i.e. TC1, TC2, and TC3) are nearly parallel to one another for a notable range of temperature below liquidus temperature T_L . Thus, the

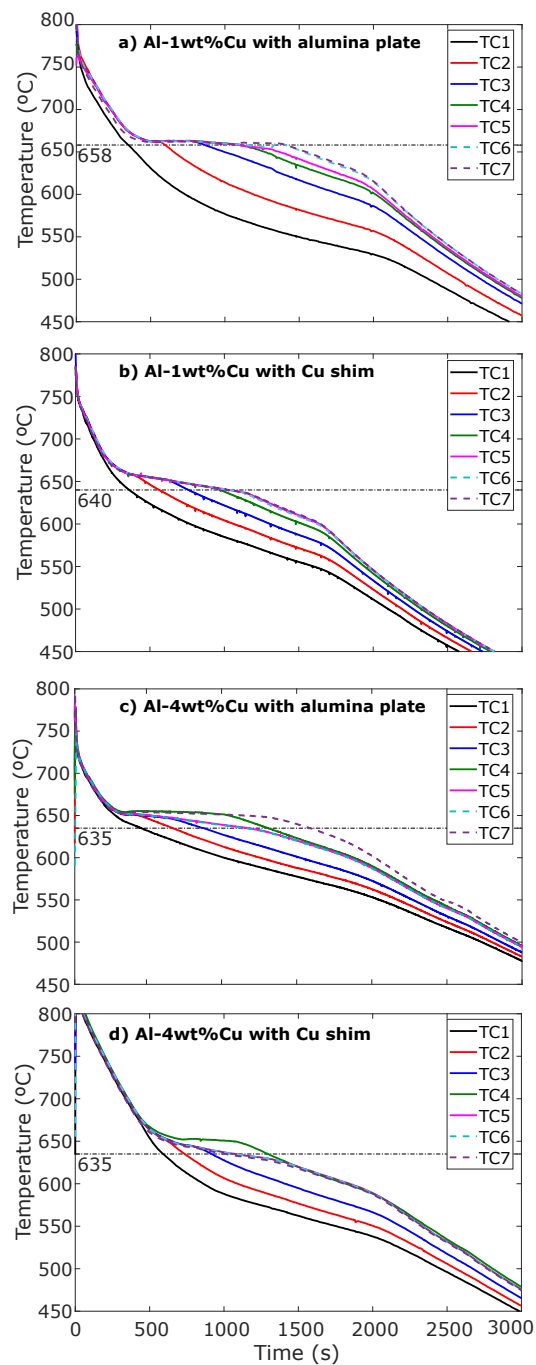


Figure 3: Temperatures measured by the 7 thermocouples during the casting experiments. Al-1 wt%Cu: (a) with the alumina plate between the mold and the chill plate and (b) with direct contact between the mold and the chill plate. Al-4 wt%Cu: (c) with the alumina plate between the mold and the chill plate and (d) with direct contact between the mold and the chill plate. Horizontal dash-dot lines mark the temperature at which the velocity of isotherms was estimated.

velocity of isotherms at $T = T_L^- \lesssim T_L$ (dash-dot lines in Fig. 3) — calculated as $V \approx d_{12}/(t_2 - t_1)$, with d_{12} the distance between TC1 and TC2, and t_1 and t_2 the times at which TC1 and TC2 respectively cross the temperature T_L^- — provides a reasonably accurate estimation of the average solidification front velocity between TC1 and TC2.

The local temperature gradient is less straightforward to obtain, as it depends significantly on the method used to calculate it. As explained in Section 2.1.3, it is calculated from the time-averaged slopes of TC1 and TC2 between t_1 and t_2 .

Resulting solidification conditions between TC1 and TC2 are summarized in Table 1. In the simulations, we specifically focus on the two experiments performed with an insulating alumina plate, i.e. cases (a) and (c) in Fig. 3 and Table 1.

Case	V ($\mu\text{m/s}$)	G (K/mm)	R (K/s)
(a)	0.16 ± 0.01	0.91 ± 0.29	0.15 ± 0.04
(b)	0.23 ± 0.02	0.50 ± 0.01	0.12 ± 0.03
(c)	0.19 ± 0.01	0.37 ± 0.12	0.07 ± 0.02
(d)	0.28 ± 0.02	0.50 ± 0.20	0.14 ± 0.04

Table 1: Solidification velocity V , temperature gradient G , and cooling rate R between thermocouples TC1 and TC2: Al-1 wt%Cu alloy (a) with and (b) without alumina plate between mold and chill plate; Al-4 wt%Cu alloy (c) with and (d) without alumina plate between mold and chill plate.

3.2. Microstructure characterization

Cross-section micrographs between TC1 and TC2 appear in Fig. 4 for the two alloys solidified using the alumina plate between mold and chill plate.

Figure 5 shows the [100] pole figures from EBSD analysis of the dendrite orientation with respect to the cutting plane in $16 \times 4 \text{ mm}^2$ cross-section areas. We assumed that dendrites grow along their [100] crystalline direction, since they are in a well-developed dendritic regime, far from a cellular-to-dendritic transition regime in which a deviation may exist between [100] and growth direction [92, 93].

For the Al-1 wt%Cu alloy, between TC3 and TC4 the cutting plane was nearly normal to the [100] direction (Fig. 5b) but closer to the chill plate, e.g. between TC1 and TC2, the misorientation was more notable (Fig. 5a). In the Al-4 wt%Cu alloy (Fig. 4b), most cross-sections presented several grains of different orientations with no remarkable preferential orientation (Fig. 5c).

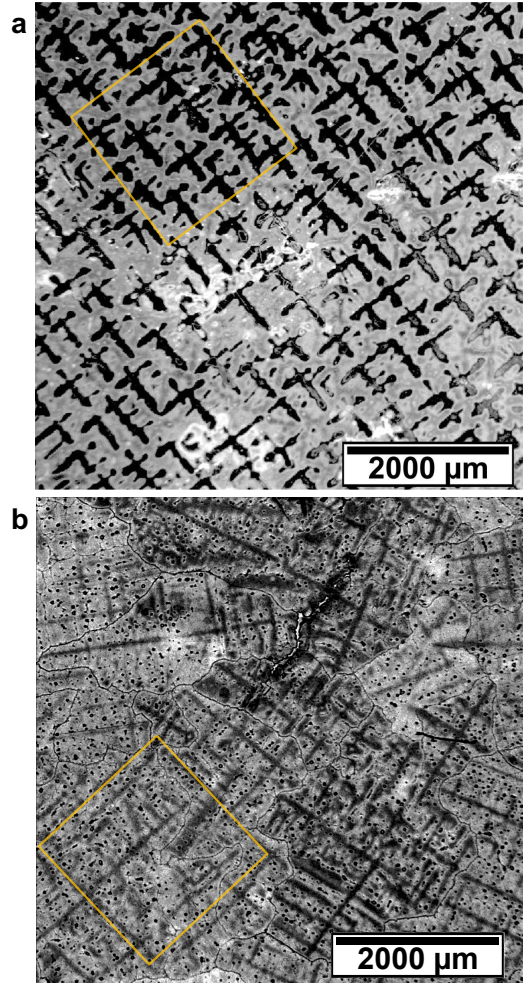


Figure 4: Micrographs of the cross-section of the (a) Al-1 wt% Cu and (b) Al-4 wt% Cu alloy solidified using the alumina plate between the mold and the chill plate at the midpoint between thermocouples 1 and 2. Orange squares show the regions compared to simulation results in Fig. 11.

We used the Euler angle Φ to estimate the deviation between the apparent spacing in the cross-sections λ_m and the actual spacing normal to the growth direction $\lambda \approx \cos(\Phi)\lambda_m$ (Fig. 6). The angle Φ , negligible for most grains between TC3 and TC4 in the Al-1 wt%Cu alloy, reached up to 40° between TC1 and TC2 and in the the Al-4 wt%Cu alloy, thus leading to λ up to 25% lower than λ_m . Hence, for all samples, we estimated $\lambda \approx 0.9\lambda_m$ as an average approximate angle correction.

The average measured and corrected PDAS are plotted as a function of the cooling rate R in Fig. 7 (Al-1 wt%Cu) and Fig. 8 (Al-4 wt%Cu), together with literature data for relevant composition ranges

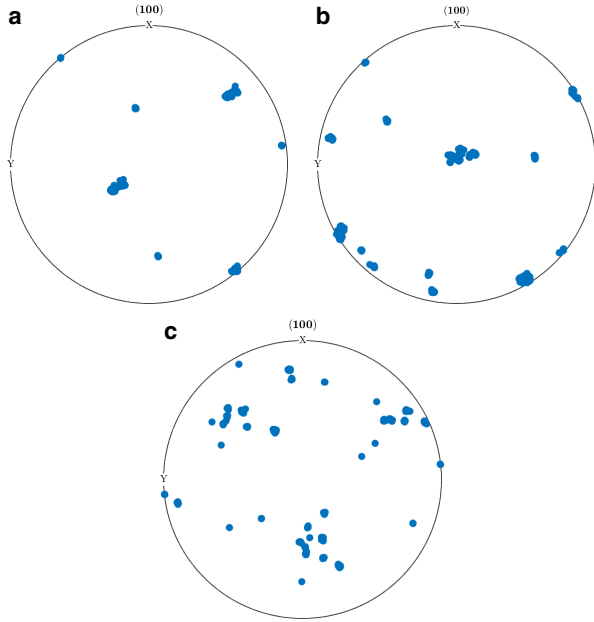


Figure 5: EBSD [100] pole figures for the Al-1 wt% Cu alloy (a) between TC1 and TC2 and (b) between TC3 and TC4 as well as (c) for the Al-4 wt% Cu between TC3 and TC4. The scatter in a and c shows the lack of overall alignment of the [100] dendrite growth direction with the observation plane, in contrast to panel b showing a higher density of grains growing along the principal temperature gradient direction.

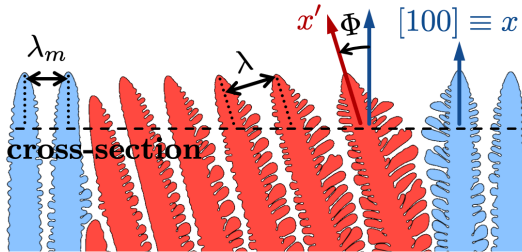


Figure 6: Schematic for the correction of the dendrite spacing from the dendrite orientation, where λ_m is the PDAS measured on the cross-section and λ is the actual PDAS.

(see graph legend), and a dotted line illustrating a $R^{-0.5}$ slope.

Even though PDAS were slightly lower when the mold was in direct contact with the chill plate, this effect was relatively small because the two achieved cooling rates remained of the same order (see Fig. 3), which was not sufficient to yield a significant change microstructural length scale. Therefore, in Figs 7 and 8, we did not distinguish between experiments with and without the insulating alumina plate, since the resulting scatter is negligible compared to the overall cloud of points.

Table 2: Fitted tip radii and selection parameters from the PF simulations of the Al-1 wt%Cu alloy at $V = 160 \mu\text{m/s}$ and $G = 10^2 \text{ K/m}$.

λ (μm)	ρ (μm)	σ
336	8.94	0.0605
387	8.93	0.0606
438	8.83	0.0619
490	9.09	0.0585
505	9.06	0.0589
521	9.02	0.0593

3.3. Simulations

The first quantitative results extracted from the PF simulation are the dendrite tip radii and the corresponding tip selection parameter σ . Results from simulations of the Al-1 wt%Cu alloy at $V = 160 \mu\text{m/s}$ and $G = 10^2 \text{ K/m}$ for different spacings λ appear in Table 2. The average radius remains within $\rho = 8.96 \pm 0.13 \mu\text{m}$, with less than 4% difference between radii measured in the y and z directions. The resulting tip selection parameter, accounting for the tip temperature, i.e. for the temperature-dependent capillarity length, is within $\sigma = 0.06 \pm 0.002$. This compares well with linear solvability theory, which gives $\sigma \approx 0.06$ for a one-sided model (see, e.g., Fig. 2 of Ref. [94] with $\alpha = 15\epsilon_4 = 0.18$ and Eq. (4.3) therein with $\mu = 0$). In the DNN simulations we used $\sigma = 0.063$, which was extracted from preliminary PF simulations performed before we obtained all PF results. However, we expect that such small difference had little influence on any of our results and conclusions.

For both PF and DNN models, results of single-spacing simulations appear in Figs 9 (Al-1 wt%Cu) and 10 (Al-4 wt%Cu), showing (a) primary tip undercooling versus spacing within the stable PDAS range, as well as (b-c) typical primary dendrites within the stable range and their surrounding solute field in a (010) plane. We also report the calculated values of λ_{min} , λ_{max} , as well as the ratio $\lambda_{max}/\lambda_{min}$ for all simulations in Table 3 (Al-1 wt%Cu) and Table 4 (Al-4 wt%Cu).

Final microstructures in the spatially extended simulations are illustrated and compared to experimental micrographs in Fig. 11 for the Al-1 wt%Cu (a-c) and the Al-4 wt%Cu (d,e) alloys, superimposed with a Delaunay triangulation similar to the one used to calculate average primary spacings. Average spacings $\langle \lambda \rangle$ from simulations are reported in Figs 7 and 8 as thick crosses (\otimes), together with

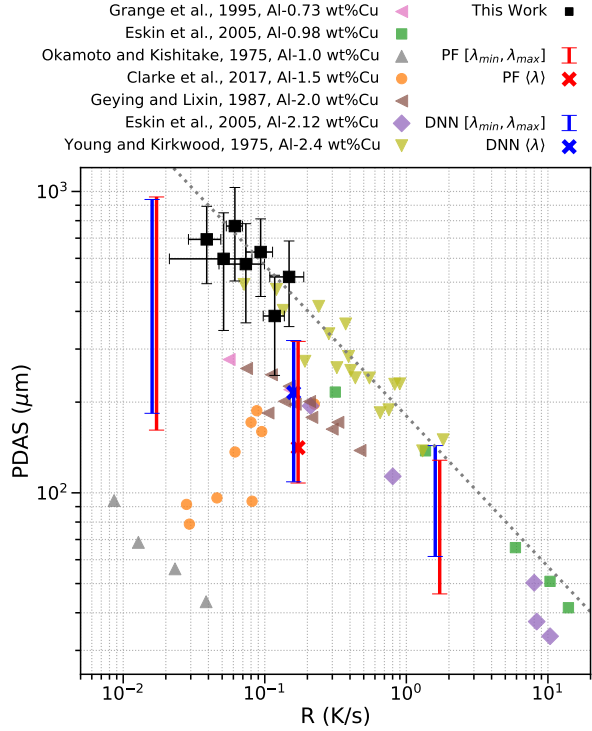


Figure 7: Comparison of PDAS as a function of cooling rate for the Al-1 wt%Cu alloy in our experiments (both cooling conditions), together with literature results, as well as PF (red) and DNN (blue) predictions of dendritic stability range (error bars) and average spacing in spatially extended dendritic arrays (\star). PF and DNN simulations are performed at the same (G, V) and hence R , but PF data points in the plot are slightly shifted to the right, for the sake of readability.

Table 3: Predicted spacing stability limits and ratio $\lambda_{max}/\lambda_{min}$ from PF and DNN simulations of Al-1 wt%Cu solidification at $V = 160 \mu\text{m/s}$.

G (K/m)		10^2	10^3	10^4
λ_{min} (μm)	PF	161.5	107.8	46.2
	DNN	183.6	108.8	61.5
λ_{max} (μm)	PF	959.0	318.1	128.3
	DNN	940.7	320.2	143.5
$\lambda_{max}/\lambda_{min}$	PF	5.94	2.95	2.78
	DNN	5.12	2.94	2.33

predicted stability ranges as vertical error bars.

In terms of computational performance (see brief discussion in the Supplementary Material), a representative simulation in the vicinity of $\lambda \approx \lambda_{min}$ at $G = 10^3$ K/m for the Al-1 wt%Cu alloy, performed on the same hardware (one NVIDIA GeForce[®] GTX 1080Ti and a single core of an Intel[®] i7-6850K) was performed about six times faster with

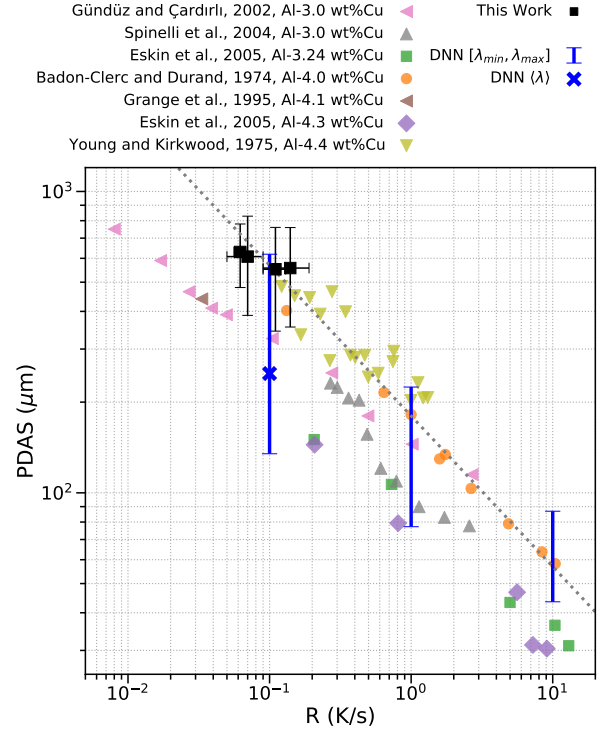


Figure 8: Comparison of PDAS as a function of cooling rate for the Al-4 wt%Cu alloy in our experiments (both cooling conditions), together with literature results, and DNN (blue) predictions of dendritic stability range (error bars) and average spacing in a spatially extended dendritic array (\star).

Table 4: Predicted spacing stability limits and ratio $\lambda_{max}/\lambda_{min}$ from DNN simulations of the Al-4 wt%Cu alloy at $V = 200 \mu\text{m/s}$.

G (K/m)	5×10^2	5×10^3	5×10^4
λ_{min} (μm)	134.8	77.2	43.5
λ_{max} (μm)	619.2	224.4	86.9
$\lambda_{max}/\lambda_{min}$	4.59	2.88	1.99

DNN than PF. However, in this regime where both PF and DNN simulations are achievable, DNN simulations are far outside of their optimal performance, which can only be obtained when $\rho \ll D/V$ and PF simulations become unfeasible.

4. Discussion

4.1. Experiments

The thermocouples farthest from the chill plate, namely TC5, TC6, and TC7 provide an estimation of the vertical thermal gradient. The temperatures

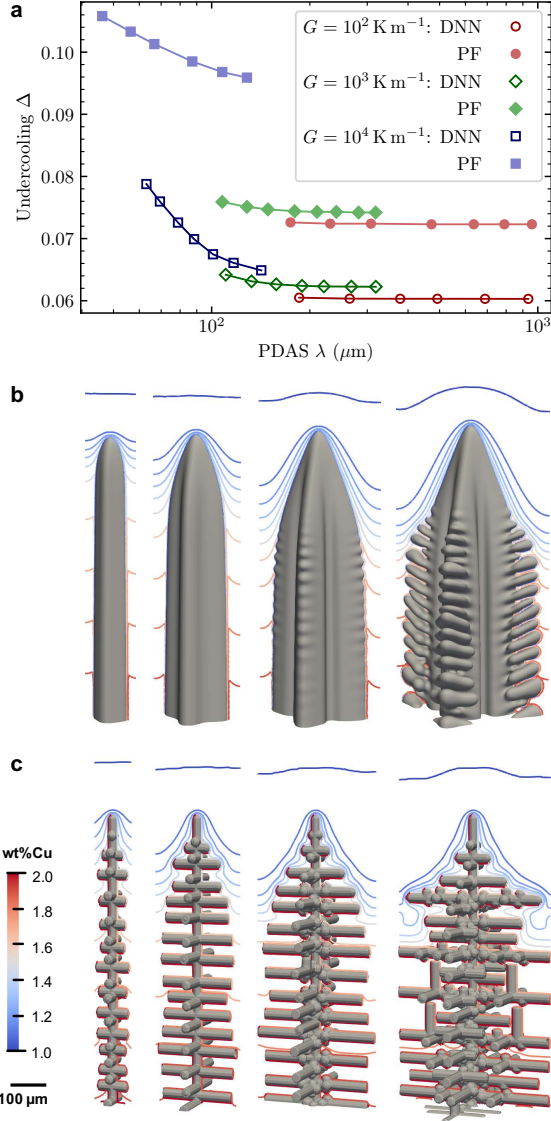


Figure 9: Simulation results for PDAS stability range for the Al-1 wt%Cu alloy at $V = 160 \mu\text{m/s}$: (a) Steady-state primary tip undercooling Δ versus λ , showing only the stable spacings $\lambda_{min} < \lambda < \lambda_{max}$ predicted by PF (full symbols) and DNN (open symbols) models for $G = 10^2$ (red), 10^3 (green), and 10^4 K/m (blue), and dendrite morphologies simulated with (b) PF and (c) DNN models for stable spacings $\lambda \approx 110, 180, 250,$ and $320 \mu\text{m}$ (left to right) for $G = 10^3$ K/m. Panels (b) and (c) appear at the same scale, showing the solid-liquid interface and similar iso-concentration lines (wt%Cu) in a (010) plane. In panel (a), the leftmost and rightmost data points show the lowest (λ_{min}) and highest (λ_{max}) stable spacings identified for each set of parameters, even though within the stability range only a small subset of the simulations are shown as symbols for the sake of readability.

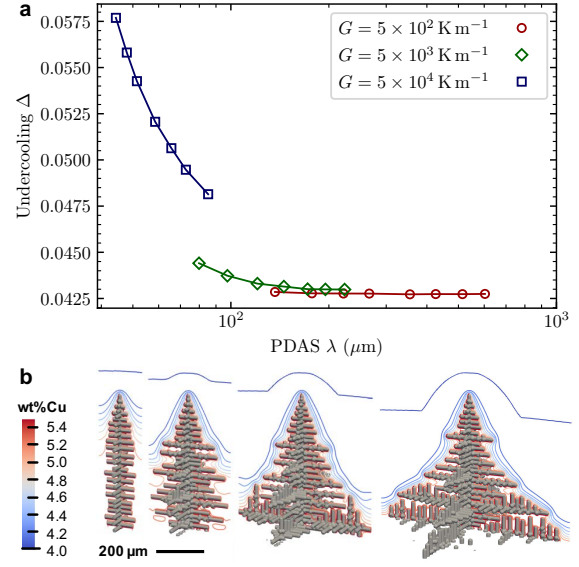


Figure 10: Simulation results for PDAS stability range for the Al-4 wt%Cu alloy at $V = 200 \mu\text{m/s}$: (a) Steady-state primary tip undercooling Δ versus PDAS, showing only the stable spacings $\lambda_{min} < \lambda < \lambda_{max}$ predicted by the DNN simulations for $G = 5 \times 10^2$ (red), 5×10^3 (green), and 5×10^4 K/m (blue), and (b) view of the dendrite morphologies for stable spacings $\lambda \approx 137, 296, 454,$ and $603 \mu\text{m}$ (left to right) for $G = 5 \times 10^2$ K/m, showing the solid-liquid interface and iso-concentration lines (wt%Cu) in a (010) plane. In panel (a), the leftmost and rightmost data points show the lowest (λ_{min}) and highest (λ_{max}) stable spacings identified for each set of parameters, even though within the stability range only a small subset of the simulations are shown as symbols for the sake of readability.

of TC6 and TC7 mostly overlap, except in the Al-4 wt%Cu case with alumina plate (Fig. 3a), where TC7 is at a slightly higher temperature. This is likely due to a second solidification front moving from the opposite end of the mold and promoting earlier solidification of that region. Something similar occurs in the Al-4 wt%Cu alloy when the mold is in direct contact with the chill plate (Fig. 3d): TC5 to TC7 exhibit a faster initial cooling rates than TC4 until the temperatures converge, suggesting that solidification occurs around the same time in this region. This uncertainty in the temperature distribution and history makes it more challenging to establish a clear processing-microstructure relationship in this central region of the mold. Therefore, we chose to focus primarily on the solidification behavior between TC1 and TC2, where the solidification conditions can be estimated with greater confidence.

Dendritic arrays have a more regular arrange-

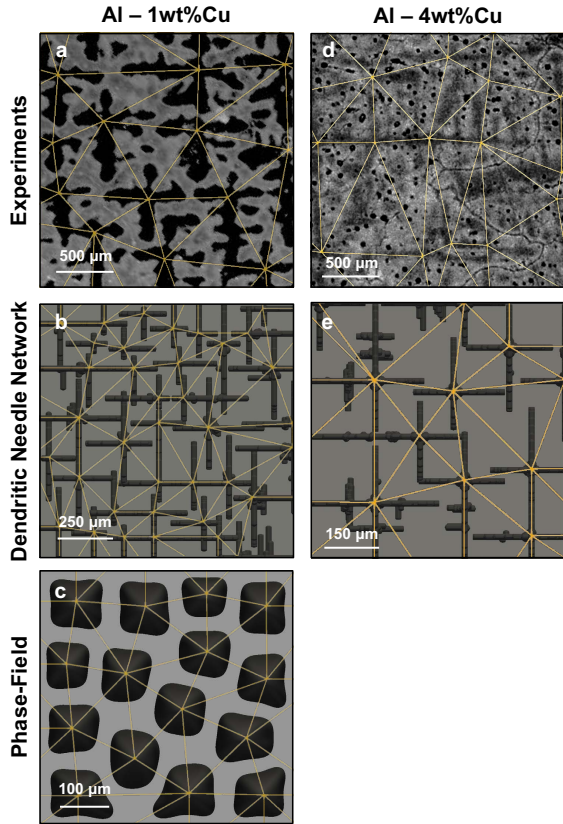


Figure 11: Experimental micrographs (a,d) and steady state microstructures observed in the (x -) direction simulated using the DNN (b,e) and PF (c) methods for the Al-1 wt%Cu (a-c) and the Al-4 wt%Cu (d,e) alloy processed in the presence of an insulating alumina plate between the mold and the chill face, i.e. for $V = 160 \mu\text{m/s}$ and $G = 10^3 \text{ K/m}$ for Al-1 wt%Cu (a-c) and $V = 200 \mu\text{m/s}$ and $G = 5 \times 10^2 \text{ K/m}$ for Al-4 wt%Cu (d,e).

ment and a better defined microstructure in the micrographs of the central region of the mold (i.e. between TC2 and TC3, or TC3 and TC4) than near the chill plate (i.e. between TC1 and TC2) in the Al-1 wt%Cu alloy (see Fig. 5). This is likely a sign of transient thermal conditions at the beginning of solidification. Moreover, the insulation of the mold is poorer near the chill face, leading to possible heat fluxes in different directions, such that the dendrites growth direction may deviate from the main thermal gradient direction. Further away from the chill plate, the solidification front is stabilized and these disturbances vanish for the most part. In spite of these transient conditions, microstructures between TC1 and TC2 are sufficiently defined to extract a reasonable measure of the PDAS.

The expected power law dependence of the PDAS with the cooling rate R appears in Figs 7 and 8, as the data follows the illustrated $R^{-0.5}$ slope suggested in earlier studies [36–47, 95]. While our experiments did not permit to scan an extensive range of cooling rates, they still suggest a decrease in PDAS for higher cooling rate, consistently with this $\lambda \sim R^{-0.5}$ power law.

For the Al-4 wt%Cu alloy, our measured PDAS coincide well with the results of [40, 42, 95] for similar cooling rates. However, our measurements for both alloys appear on the higher end of the measured spacing distribution from the literature for comparable compositions. They also appear on the high end of the calculated stable ranges. This may be attributed to several factors.

First, the representation of λ as a sole function of R is a simplification. For a given alloy, the average PDAS is a function of both G and R , such that, for a given cooling rate $R = G \times V$, different sets of points might represent substantially different conditions and even different growth regimes. A better representation would be a three-dimensional graph with axes λ , G , and V (or even 4D including c_∞).

Second, experimental setups and configurations compared here differ substantially from one another. Most previous data comes from thin-sample or Bridgman directional solidification experiments. Even among these, whether the solidification is horizontal, vertical upwards, or vertical downwards, has important consequences, particularly in terms of thermo-solutal convection [96–102]. For example, in the experiments from Ref. [68] (full orange circles in Fig. 7), performed vertically upwards, it was shown that, in spite of the low sample thickness ($200 \mu\text{m}$), the extent of convection was sufficient for these experiments to occur within a cellular-to-dendritic transition regime, explaining the inverse trend with $\partial\lambda/\partial R > 0$ in Fig. 7 [68], in place of the expected $\lambda \sim R^{-0.5}$ in the fully dendritic regime.

Third, we relied on limited local thermocouple measurements, which arguably leaves room for error in the estimation of the local (G, V) conditions at exact times and locations within the mold. A more accurate estimation of the local temperature profile in the sample could be achieved, for instance extending our multiscale modeling approach to thermal and solutal transport simulations at the macroscopic scale, which is the focus of an ongoing follow-up study.

Finally, we based our estimation of the PDAS on two-dimensional cross-sections. Even though we

attempted to correct for the misorientation of the dendrite growth direction, we expect that underlying assumptions also lead to some amount of error in the PDAS measurements. Such issues could be tackled in further studies using three-dimensional visualization methods, such as X-ray tomography [103–107], which would provide an unambiguous representation of dendritic arrays and spacings.

4.2. Simulations

For the Al-1 wt%Cu alloy, the calculated values for λ_{min} and λ_{max} exhibit a striking agreement between PF and DNN methods, in spite of the lower undercooling predicted by DNN compared to PF (Fig. 9a), which was already observed and reported in an ongoing benchmark study [108]. Some discrepancy between DNN and PF appears at higher undercooling (i.e. for $G = 10^4$ K/m in Fig. 9a), which we attribute to the fact that a higher G promotes a transition toward an intermediate regime between cellular and dendritic. Consequently, the agreement is best at low G , when microstructures are well-developed dendrites made of thin hierarchical branches, for which the DNN model was specifically designed. For both compositions and both simulation methods, the dependence of both λ_{min} and λ_{max} fall close to the phenomenological $R^{-0.5}$ power law (dotted lines in Figs 7 and 8).

Hence, the ratio $\lambda_{max}/\lambda_{min}$ (Tables 3 and 4) also presents a striking agreement between the two simulation methods. This ratio is as high as 5 or 6 for the lowest values of G , and decreases consistently with increasing G , as microstructures approach an intermediate cellular-dendritic regime. The fact that $\lambda_{max}/\lambda_{min}$ is much higher than 2 is consistent with recent studies [68, 90, 91, 109] and in contrast with earlier theories, which suggested that $\lambda_{max}/\lambda_{min} \approx 2$ [23, 24], but mostly by lack of a proper simulation method to study branching instability at $\lambda \approx \lambda_{max}$. The decrease in $\lambda_{max}/\lambda_{min}$ with G and the fact that it may tend toward 2 as the gradient increases are new observations that warrant further investigation.

Overall, this comparison between simulations and experiments, in conditions relevant to industrial casting, provides a compelling demonstration that physics-based models can be coupled across scales to yield quantitative predictions of key microstructural length scales — here specifically illustrated for the PDAS. However, our simulations, while in good agreement with literature data, seem

to underestimate the spacings measured in our experiments. This is due to error sources in both simulations and experiments, such that some limitations in the current calculations and assumptions deserve to be discussed, as they point toward directions for improvement and further research.

First, it was previously shown that a microstructural steady state, with a fixed PDAS, may require a substantially longer time than that required to reach a steady undercooling and growth velocity of the solidification front [68]. Hence, even though microstructures may appear at steady state, a slow interaction and elimination process might still be occurring, possibly leading to an increase of average spacing at longer time scale.

Then, in the single-spacing simulations, we made the assumption of a quincux (fcc-like) spatial order of the dendritic arrays (Fig. 2). As such, these simulations are only representative of λ_{min} and λ_{max} in a perfectly ordered array with this specific arrangement. This ordering can be identified in terms of nearest neighbors as an irregular hexagonal pattern (dotted line in Fig. 2), with two longer edges along the directions corresponding to side-branches growth. It was shown to be predominant in directionally solidified single crystals (see, e.g., the high density of such irregular hexagons in the bottom left region of Fig. 2b in Ref. [110]) — in contrast to predominantly regular hexagonal arrays in cellular growth due to the axisymmetry of cells [33, 111]. While we chose to leave this aspect out of the scope of the current study, it would be interesting, among future directions, to investigate the influence of the spatial order on the resulting spacing stability range, as well as the possible transition from regular to irregular hexagonal arrays with the appearance of side-branches between cellular and dendritic growth regimes.

In both experiments and spatially extended simulations, spatial order of the array is never perfect. In the experiments, array disorder is primarily promoted by the inhomogeneous processing conditions, with gradients in G , V , and c_∞ due to a large extent to convection, and the fact that microstructures are polycrystalline, thus leading to sustained elimination and branching events [90, 112].

Due to this disorder, a more advanced algorithm than our Delaunay triangulation could have led to a more accurate PDAS estimation [110, 113–115]. However, we expect that such methods would have only filtered a handful of nearest neighbor outliers, such that the resulting correction would have been

minimal once reported within the nearly two orders of magnitude of PDAS variation discussed here (Figs 7-8).

In all simulations, we made the assumptions that G and V are constant, that heat transport is infinitely fast compared to solute transport, and that solute transport occurs primarily by diffusion in the liquid phase. While these are all reasonable assumptions for the solidification of a metallic system considered at a scale lower than the characteristic hydrodynamic length, we expect that such assumptions introduce some amount of discrepancy by deviating from exact experimental conditions.

Finally, one intrinsic limitation of the DNN model is that primary dendrite trunks cannot drift laterally, such that spacings can only be adjusted through elimination and branching events. This leads to a distribution of spacing less homogeneous than in both experiments and PF simulations (Fig. 11), as already noted for thin-sample solidification of Al-Si alloys [109]. The DNN model might be adapted to allow such a drifting, but this would require (1) a new mathematical formulation of the FIF that would incorporate the directionality of the incoming solute flux, (2) establishing laws for dendrite drifting velocities in inhomogeneous arrays, and (3) a notably more complex implementation.

In spite of these limitations, the present comparison between experiments and simulations highlights a promising pathway toward quantitative predictions of microstructural length scales (e.g. PDAS) in casting processes. The striking agreement between PF and DNN predictions is a strong indication that discrepancies between simulated and experimental data stem from the fundamental assumptions behind the models rather than from the upscaling from PF to DNN simulations.

5. Summary and perspectives

In this article, we demonstrated that primary dendritic spacings in metallic alloys cast in industrially relevant conditions can be calculated by directly combining physics-based models — with barely any adjustable parameters. On the one hand, we performed casting experiments of Al-Cu alloys and related the cooling conditions measured by thermocouples to the PDAS measured from cross-sections micrographs. On the other hand, we calculated PDAS stability ranges and simulated entire dendritic arrays using two different methods, namely phase-field (PF) and den-

ditric needle network (DNN) models. For the alloy with lower copper content (Al-1 wt%Cu), both types of simulations are feasible, and they lead to very similar results. For the more concentrated alloy (Al-4 wt%Cu), the wide separation of scale between dendrite tip radius ρ and diffusion length l_D makes PF simulations prohibitively challenging, while DNN simulations still yield a good agreement with experiments.

We compared our results to the extensive body of literature on PDAS selection in Al-Cu alloys (see Fig. I in the Supplementary Material), and found an overall good agreement between our results and published data. It is, to our knowledge, the first time that this broad data set was compiled and directly compared to simulation predictions. The agreement between simulations and experimental data provides a conclusive validation of the models' capability to reliably predict primary spacings. Moreover, in spite of a slight underestimation of undercooling by the DNN method as compared to PF (already identified elsewhere [108]), the excellent agreement in terms of stable spacing ranges for different sets of parameters provides a further validation of the models. In summary, we have shown that quantitative PF simulations, computationally limited to dilute alloys, could be readily extended to more concentrated alloys using the DNN approach. This opens the way to further direct comparisons of experiments and simulations at experimentally relevant length and time scales.

Perspectives from this work are manyfold. From a fundamental standpoint, the relationship between the width of the PDAS stability range (i.e. the ratio $\lambda_{max}/\lambda_{min}$) and the temperature gradient remains to be explored in further details. From an ICME perspective, ongoing works include the extension of this multiscale modeling strategy toward both the macroscopic scale — e.g. coupling to thermomechanical simulations of the process with possible integration of convection into DNN simulations [84, 85] — and toward the nanoscale — e.g. calculating phase diagrams from first principles [116, 117] and solid-liquid interface properties from molecular dynamics [118, 119]. Such computational frameworks could also be complemented by similar multi-scale strategies for later processing steps, e.g. including the formation of secondary phases such as precipitates [120, 121].

Acknowledgements

This research was funded by the European Research Council Advanced Grant VIRMETAL under the European Union's Horizon 2020 research and innovation programme (Grant Agreement 669141). D.T. acknowledges support from the European Union's Horizon 2020 research and innovation programme through a Marie Skłodowska-Curie Individual Fellowship (Grant Agreement 842795). Additional support from the HexaGB project of the Spanish Ministry of Science (reference RTI2018-098245) is also gratefully acknowledged. B.B. acknowledges support by the Spanish Ministry of Education through the Fellowship FPU15/00403 and D.T. and J.L.L. also gratefully acknowledge support by the NVIDIA Corporation with the donation of two Titan Xp GPUs. O.M.W. and M.S.T. would like to acknowledge Purdue University for supporting this work through start-up funds. The valuable help from undergraduate students Jesús Martínez Justo and Luis Montes Mota (Polytechnic University of Madrid) for the metallography sample preparation is also gratefully acknowledged.

References

- [1] M. C. Flemings, Solidification processing, *Metallurgical transactions* 5 (10) (1974) 2121–2134.
- [2] W. Kurz, D. J. Fisher, R. Trivedi, Progress in modelling solidification microstructures in metals and alloys: dendrites and cells from 1700 to 2000, *International Materials Reviews* 64 (6) (2019) 311–354.
- [3] R. Trivedi, W. Kurz, Dendritic growth, *International Materials Reviews* 39 (2) (1994) 49–74.
- [4] J. M. Quaresma, C. A. Santos, A. Garcia, Correlation between unsteady-state solidification conditions, dendrite spacings, and mechanical properties of Al-Cu alloys, *Metallurgical and Materials Transactions A* 31 (12) (2000) 3167–3178.
- [5] W. R. Osório, A. Garcia, Modeling dendritic structure and mechanical properties of Zn-Al alloys as a function of solidification conditions, *Materials Science and Engineering: A* 325 (1-2) (2002) 103–111.
- [6] W. R. Osorio, P. R. Goulart, A. Garcia, G. A. Santos, C. M. Neto, Effect of dendritic arm spacing on mechanical properties and corrosion resistance of Al 9 wt pct Si and Zn 27 wt pct Al alloys, *Metallurgical and Materials Transactions A* 37 (8) (2006) 2525–2538.
- [7] C. Beckermann, Modelling of macrosegregation: applications and future needs, *International Materials Reviews* 47 (5) (2002) 243–261.
- [8] W. R. Osório, C. M. Freire, A. Garcia, The effect of the dendritic microstructure on the corrosion resistance of Zn-Al alloys, *Journal of Alloys and Compounds* 397 (1-2) (2005) 179–191.
- [9] W. Osório, J. Spinelli, I. Ferreira, A. Garcia, The roles of macrosegregation and of dendritic array spacings on the electrochemical behavior of an Al-4.5 wt.% Cu alloy, *Electrochimica Acta* 52 (9) (2007) 3265–3273.
- [10] R. Nasser-Rafi, R. Deshmukh, D. R. Poirier, Flow of interdendritic liquid and permeability in Pb-20 wt pct Sn alloys, *Metallurgical Transactions A* 16 (12) (1985) 2263–2271.
- [11] D. R. Poirier, Permeability for flow of interdendritic liquid in columnar-dendritic alloys, *Metallurgical Transactions B* 18 (1) (1987) 245–255.
- [12] S. Ganesan, C. Chan, D. R. Poirier, Permeability for flow parallel to primary dendrite arms, *Materials Science and Engineering: A* 151 (1) (1992) 97–105.
- [13] R. Santos, M. Melo, Permeability of interdendritic channels, *Materials Science and Engineering: A* 391 (1-2) (2005) 151–158.
- [14] T. Takaki, S. Sakane, M. Ohno, Y. Shibuta, T. Aoki, Permeability prediction for flow normal to columnar solidification structures by large-scale simulations of phase-field and lattice Boltzmann methods, *Acta Materialia* 164 (2019) 237–249.
- [15] J. S. Langer, Instabilities and pattern formation in crystal growth, *Reviews of modern physics* 52 (1) (1980) 1.
- [16] E. Ben-Jacob, N. Goldenfeld, B. Kotliar, J. Langer, Pattern selection in dendritic solidification, *Physical review letters* 53 (22) (1984) 2110.
- [17] M. Ben Amar, E. Brener, Theory of pattern selection in three-dimensional nonaxisymmetric dendritic growth, *Physical review letters* 71 (4) (1993) 589.
- [18] E. Brener, Needle-crystal solution in three-dimensional dendritic growth, *Physical review letters* 71 (22) (1993) 3653.
- [19] A. Karma, Y. H. Lee, M. Plapp, Three-dimensional dendrite-tip morphology at low undercooling, *Physical Review E* 61 (4) (2000) 3996.
- [20] K. Somboonsuk, R. Trivedi, Dynamical studies of dendritic growth, *Acta Metallurgica* 33 (6) (1985) 1051–1060.
- [21] R. Trivedi, K. Somboonsuk, Pattern formation during the directional solidification of binary systems, *Acta metallurgica* 33 (6) (1985) 1061–1068.
- [22] W. Kurz, D. J. Fisher, Dendrite growth at the limit of stability: tip radius and spacing, *Acta Metallurgica* 29 (1) (1981) 11–20.
- [23] S.-Z. Lu, J. Hunt, A numerical analysis of dendritic and cellular array growth: the spacing adjustment mechanisms, *Journal of Crystal Growth* 123 (1-2) (1992) 17–34.
- [24] J. Hunt, S.-Z. Lu, Numerical modeling of cellular/dendritic array growth: spacing and structure predictions, *Metallurgical and Materials Transactions A* 27 (3) (1996) 611–623.
- [25] J. A. Warren, J. Langer, Prediction of dendritic spacings in a directional-solidification experiment, *Physical Review E* 47 (4) (1993) 2702.
- [26] S. H. Han, R. Trivedi, Primary spacing selection in directionally solidified alloys, *Acta Metallurgica Et Materialia* 42 (1) (1994) 25–41.
- [27] H. Weidong, G. Xingguo, Z. Yaohe, Primary spacing selection of constrained dendritic growth, *Journal of crystal growth* 134 (1-2) (1993) 105–115.
- [28] R. Trivedi, W. Kurz, Solidification microstructures: A conceptual approach, *Acta Metallurgica et Materialia* 42 (1) (1994) 15–23.
- [29] W. Kurz, D. J. Fisher, Fundamentals of solidification,

- Trans Tech Publ, 1989.
- [30] J. Hunt, Solidification and casting of metals, The Metal Society, London 3.
- [31] W. J. Boettinger, S. R. Coriell, A. L. Greer, A. Karma, W. Kurz, M. Rappaz, R. Trivedi, Solidification microstructures: recent developments, future directions, *Acta Materialia* 48 (2000) 43–70.
- [32] N. Provatas, K. Elder, *Phase-Field Methods in Materials Science and Engineering*, Wiley-VCH Verlag GmbH & Co., 2010.
- [33] D. Tourret, J.-M. Debierre, Y. Song, F. L. Mota, N. Bergeon, R. Guerin, R. Trivedi, B. Billia, A. Karma, Oscillatory cellular patterns in three-dimensional directional solidification, *Physical Review E* 92 (4) (2015) 042401.
- [34] D. Tourret, A. Karma, Growth competition of columnar dendritic grains: A phase-field study, *Acta Materialia* 82 (2015) 64–83.
- [35] A. Geying, L. Lixin, Dendrite Spacing in Unidirectionally Solidified Al-Cu Alloy, *Journal of Crystal Growth* 80 (1987) 383–392.
- [36] D. G. McCartney, J. D. Hunt, Measurements of Cell and Primary Dendrite, *Acta Metallurgica* 29 (11) (1981) 1851–1863.
- [37] X. Lin, W. Huang, J. Feng, T. Li, Y. Zhou, History-dependent selection of primary cellular/dendritic spacing during unidirectional solidification in aluminum alloys, *Acta Materialia* 47 (11) (1999) 3271–3280.
- [38] M. Gündüz, E. Çadırlı, Directional solidification of aluminium-copper alloys, *Materials Science and Engineering: A* 327 (2) (2002) 167–185.
- [39] T. Okamoto, K. Kishitake, Dendritic structure in unidirectionally solidified aluminum, tin, and zinc base binary alloys, *Journal of Crystal Growth* 29 (2) (1975) 137 – 146.
- [40] K. P. Young, D. H. Kerkwood, The dendrite arm spacings of aluminum-copper alloys solidified under steady-state conditions, *Metallurgical Transactions A* 6 (1975) 197–205.
- [41] J. Kaneko, Dendrite coarsening during solidification of hypo-and hyper-eutectic Al-Cu alloys, *Journal of Materials Science* 12 (1977) 1392–1400.
- [42] R.-J. Su, R. A. Overfelt, W. A. Jemian, Microstructural and compositional transients during accelerated directional solidification of Al-4.5 wt pct Cu, *Metallurgical and Materials Transactions A* 29 (1998) 2375–2381.
- [43] G. Grange, J. Gastaldi, C. Jourdan, B. Billia, Evolution of characteristic pattern parameters in directional solidification of thin samples of a dilute AlCu alloy, *Journal of crystal growth* 151 (1-2) (1995) 192–199.
- [44] J. M. V. Quaresma, C. A. Santos, A. Garcia, Correlation between unsteady-state solidification conditions, dendrite spacings, and mechanical properties of Al-Cu alloys, *Metallurgical and Materials Transactions A* 31 (12) (2000) 3167–3178.
- [45] O. L. Rocha, C. A. Siqueira, A. Garcia, Heat flow parameters affecting dendrite spacings during unsteady-state solidification of Sn-Pb and Al-Cu alloys, *Metallurgical and Materials Transactions A* 34 (4) (2003) 995–1006.
- [46] J. E. Spinelli, D. M. Rosa, I. L. Ferreira, A. Garcia, Influence of melt convection on dendritic spacings of downward unsteady-state directionally solidified Al-Cu alloys, *Materials Science and Engineering: A* 383 (2) (2004) 271–282.
- [47] D. Eskin, Q. Du, D. Ruvalcaba, L. Katgerman, Experimental study of structure formation in binary Al-Cu alloys at different cooling rates, *Materials Science and Engineering A* 405 (1-2) (2005) 1–10.
- [48] M. Rappaz, M. Bellet, M. Deville, *Numerical modeling in materials science and engineering*, Vol. 32, Springer Science & Business Media, 2010.
- [49] J. Ni, C. Beckermann, A volume-averaged two-phase model for transport phenomena during solidification, *Metallurgical Transactions B* 22 (3) (1991) 349–361.
- [50] C. Wang, C. Beckermann, Equiaxed dendritic solidification with convection: Part i. multiscale/multiphase modeling, *Metallurgical and materials transactions A* 27 (9) (1996) 2754–2764.
- [51] C. Wang, C. Beckermann, Equiaxed dendritic solidification with convection: Part ii. numerical simulations for an Al-4 wt pct Cu alloy, *Metallurgical and Materials Transactions A* 27 (9) (1996) 2765–2783.
- [52] H. Combeau, M. Založnik, S. Hans, P. E. Richey, Prediction of macrosegregation in steel ingots: Influence of the motion and the morphology of equiaxed grains, *Metallurgical and materials transactions B* 40 (3) (2009) 289–304.
- [53] M. Wu, A. Ludwig, Modeling equiaxed solidification with melt convection and grain sedimentation i: Model description, *Acta Materialia* 57 (19) (2009) 5621–5631.
- [54] M. Wu, A. Ludwig, Modeling equiaxed solidification with melt convection and grain sedimentation ii. model verification, *Acta Materialia* 57 (19) (2009) 5632–5644.
- [55] D. Tourret, C.-A. Gandin, T. Volkman, D. M. Herlach, Multiple non-equilibrium phase transformations: Modeling versus electro-magnetic levitation experiment, *Acta materialia* 59 (11) (2011) 4665–4677.
- [56] D. Tourret, G. Reinhart, C.-A. Gandin, G. Iles, U. Dahlborg, M. Calvo-Dahlborg, C. Bao, Gas atomization of Al-Ni powders: Solidification modeling and neutron diffraction analysis, *Acta Materialia* 59 (17) (2011) 6658–6669.
- [57] M. Rappaz, C.-A. Gandin, Probabilistic modelling of microstructure formation in solidification processes, *Acta metallurgica et materialia* 41 (2) (1993) 345–360.
- [58] C.-A. Gandin, M. Rappaz, A coupled finite element-cellular automaton model for the prediction of dendritic grain structures in solidification processes, *Acta metallurgica et materialia* 42 (7) (1994) 2233–2246.
- [59] W. Wang, P. D. Lee, M. Mclean, A model of solidification microstructures in nickel-based superalloys: predicting primary dendrite spacing selection, *Acta materialia* 51 (10) (2003) 2971–2987.
- [60] I. Steinbach, C. Beckermann, B. Kauerauf, Q. Li, J. Guo, Three-dimensional modeling of equiaxed dendritic growth on a mesoscopic scale, *Acta Materialia* 47 (3) (1999) 971–982.
- [61] A. Viardin, M. Založnik, Y. Souhar, M. Apel, H. Combeau, Mesoscopic modeling of spacing and grain selection in columnar dendritic solidification: Envelope versus phase-field model, *Acta Materialia* 122 (2017) 386–399.
- [62] D. Tourret, A. Karma, Multiscale dendritic needle network model of alloy solidification, *Acta materialia* 61 (17) (2013) 6474–6491.
- [63] D. Tourret, A. Karma, Three-dimensional dendritic needle network model for alloy solidification, *Acta Ma-*

- terialia 120 (2016) 240–254.
- [64] D. Tourret, A. J. Clarke, S. D. Imhoff, P. J. Gibbs, J. W. Gibbs, A. Karma, Three-dimensional multiscale modeling of dendritic spacing selection during al-si directional solidification, *JOM* 67 (8) (2015) 1776–1785.
- [65] D. Tourret, A. Karma, A. J. Clarke, P. J. Gibbs, S. D. Imhoff, Three-dimensional dendritic needle network model with application to al-cu directional solidification experiments, *IOP Conference Series: Materials Science and Engineering* 84 (2015) 012082.
- [66] B. Echebarria, A. Karma, S. Gurevich, Onset of side-branching in directional solidification, *Physical Review E* 81 (2) (2010) 021608.
- [67] S. Gurevich, A. Karma, M. Plapp, R. Trivedi, Phase-field study of three-dimensional steady-state growth shapes in directional solidification, *Physical Review E* 81 (1) (2010) 011603.
- [68] A. Clarke, D. Tourret, Y. Song, S. Imhoff, P. Gibbs, J. Gibbs, K. Fezzaa, A. Karma, Microstructure selection in thin-sample directional solidification of an al-cu alloy: In situ x-ray imaging and phase-field simulations, *Acta Materialia* 129 (2017) 203–216.
- [69] W. J. Boettinger, J. A. Warren, C. Beckermann, A. Karma, Phase-field simulation of solidification, *Annual Review of Materials Research* 32 (1) (2002) 163–194.
- [70] I. Steinbach, Phase-field models in materials science, *Modelling and simulation in materials science and engineering* 17 (7) (2009) 073001.
- [71] A. Karma, D. Tourret, Atomistic to continuum modeling of solidification microstructures, *Current Opinion in Solid State and Materials Science* 20 (1) (2016) 25–36.
- [72] M. Ode, S. G. Kim, W. T. Kim, T. Suzuki, Numerical prediction of the secondary dendrite arm spacing using a phase-field model, *ISIJ international* 41 (4) (2001) 345–349.
- [73] A. Karma, W.-J. Rappel, Phase-field method for computationally efficient modeling of solidification with arbitrary interface kinetics, *Physical review E* 53 (4) (1996) R3017.
- [74] A. Karma, W.-J. Rappel, Quantitative phase-field modeling of dendritic growth in two and three dimensions, *Physical review E* 57 (4) (1998) 4323.
- [75] A. Karma, Phase-field formulation for quantitative modeling of alloy solidification, *Physical Review Letters* 87 (11) (2001) 115701.
- [76] B. Echebarria, R. Folch, A. Karma, M. Plapp, Quantitative phase-field model of alloy solidification, *Physical Review E* 70 (6) (2004) 061604.
- [77] T. Shimokawabe, T. Aoki, T. Takaki, T. Endo, A. Yamana, N. Maruyama, A. Nukada, S. Matsuoka, Peta-scale phase-field simulation for dendritic solidification on the tsubame 2.0 supercomputer, in: *Proceedings of 2011 International Conference for High Performance Computing, Networking, Storage and Analysis*, 2011, pp. 1–11.
- [78] Y. Shibuta, M. Ohno, T. Takaki, Solidification in a supercomputer: from crystal nuclei to dendrite assemblages, *Jom* 67 (8) (2015) 1793–1804.
- [79] N. Provatas, N. Goldenfeld, J. Dantzig, Efficient computation of dendritic microstructures using adaptive mesh refinement, *Physical Review Letters* 80 (15) (1998) 3308.
- [80] N. Provatas, N. Goldenfeld, J. Dantzig, Adaptive mesh refinement computation of solidification microstructures using dynamic data structures, *Journal of computational physics* 148 (1) (1999) 265–290.
- [81] M. Greenwood, K. Shampur, N. Ofori-Opoku, T. Pino-maa, L. Wang, S. Gurevich, N. Provatas, Quantitative 3d phase field modelling of solidification using next-generation adaptive mesh refinement, *Computational Materials Science* 142 (2018) 153–171.
- [82] J. Rosam, P. Jimack, A. Mullis, An adaptive, fully implicit multigrid phase-field model for the quantitative simulation of non-isothermal binary alloy solidification, *Acta Materialia* 56 (17) (2008) 4559–4569.
- [83] P. Bollada, C. E. Goodyer, P. K. Jimack, A. M. Mullis, F. Yang, Three dimensional thermal-solute phase field simulation of binary alloy solidification, *Journal of Computational Physics* 287 (2015) 130–150.
- [84] D. Tourret, M. M. Francois, A. J. Clarke, Multiscale dendritic needle network model of alloy solidification with fluid flow, *Computational Materials Science* 162 (2019) 206–227.
- [85] T. Isensee, D. Tourret, Three-dimensional needle network model for dendritic growth with fluid flow, *IOP Conference Series: Materials Science and Engineering* 861 (2020) 012049.
- [86] D. Tourret, L. Sturz, A. Viardin, M. Založnik, Comparing mesoscopic models for dendritic growth, *IOP Conference Series: Materials Science and Engineering* 861 (2020) 012002.
- [87] D. Tourret, A. Karma, A. Clarke, P. Gibbs, S. Imhoff, Three-dimensional dendritic needle network model with application to al-cu directional solidification experiments, in: *IOP Conference Series: Materials Science and Engineering*, Vol. 84, IOP Publishing, 2015, p. 012082.
- [88] D. Tourret, A. J. Clarke, S. D. Imhoff, P. J. Gibbs, J. W. Gibbs, A. Karma, Three-dimensional multiscale modeling of dendritic spacing selection during al-si directional solidification, *JOM* 67 (8) (2015) 1776–1785.
- [89] R. Hielscher, C. B. Silbermann, E. Schmidl, J. Ihlemann, Denoising of crystal orientation maps, *Journal of Applied Crystallography* 52 (5).
- [90] J. Pereda, F. Mota, L. Chen, B. Billia, D. Tourret, Y. Song, J.-M. Debierre, R. Guérin, A. Karma, R. Trivedi, et al., Experimental observation of oscillatory cellular patterns in three-dimensional directional solidification, *Physical Review E* 95 (1) (2017) 012803.
- [91] Y. Song, D. Tourret, F. Mota, J. Pereda, B. Billia, N. Bergeon, R. Trivedi, A. Karma, Thermal-field effects on interface dynamics and microstructure selection during alloy directional solidification, *Acta Materialia* 150 (2018) 139–152.
- [92] S. Akamatsu, T. Ihle, Similarity law for the tilt angle of dendrites in directional solidification of non-axially-oriented crystals, *Physical Review E* 56 (4) (1997) 4479.
- [93] J. Deschamps, M. Georgelin, A. Pocheau, Growth directions of microstructures in directional solidification of crystalline materials, *Physical Review E* 78 (1) (2008) 011605.
- [94] A. Barbieri, J. Langer, Predictions of dendritic growth rates in the linearized solvability theory, *Physical Review A* 39 (10) (1989) 5314.
- [95] M. Badon-Clerc, F. Durand, The influence of concentration and thermal conditions on the structure of basaltic dendrites in aluminum-copper alloys, *Mem.*

- Sci. Rev. Metall. 71 (7) (1974) 451–459.
- [96] R. Mathiesen, L. Arnberg, P. Bleuet, A. Somogyi, Crystal fragmentation and columnar-to-equiaxed transitions in Al-Cu studied by synchrotron x-ray video microscopy, *Metallurgical and Materials Transactions A* 37 (8) (2006) 2515–2524.
- [97] D. Ruvalcaba, R. Mathiesen, D. Eskin, L. Arnberg, L. Katgerman, In situ observations of dendritic fragmentation due to local solute-enrichment during directional solidification of an aluminum alloy, *Acta Materialia* 55 (13) (2007) 4287–4292.
- [98] S. Boden, S. Eckert, B. Willers, G. Gerbeth, X-ray radioscopic visualization of the solutal convection during solidification of a ga-30 wt pct in alloy, *Metallurgical and Materials Transactions A* 39 (3) (2008) 613–623.
- [99] N. Shevchenko, S. Boden, G. Gerbeth, S. Eckert, Chimney formation in solidifying ga-25wt pct in alloys under the influence of thermosolutal melt convection, *Metallurgical and Materials Transactions A* 44 (8) (2013) 3797–3808.
- [100] A. Bogno, H. Nguyen-Thi, A. Buffet, G. Reinhart, B. Billia, N. Mangelinck-Noël, N. Bergeon, J. Baruchel, T. Schenk, Analysis by synchrotron x-ray radiography of convection effects on the dynamic evolution of the solid-liquid interface and on solute distribution during the initial transient of solidification, *Acta Materialia* 59 (11) (2011) 4356–4365.
- [101] A. J. Clarke, D. Tournet, S. D. Imhoff, P. J. Gibbs, K. Fezzaa, J. C. Cooley, W.-K. Lee, A. Deriy, B. M. Patterson, P. A. Papin, et al., X-ray imaging and controlled solidification of Al-Cu alloys toward microstructures by design, *Advanced Engineering Materials* 17 (4) (2015) 454–459.
- [102] J. W. Gibbs, D. Tournet, P. J. Gibbs, S. D. Imhoff, M. J. Gibbs, B. A. Walker, K. Fezzaa, A. J. Clarke, In situ x-ray observations of dendritic fragmentation during directional solidification of a sn-bi alloy, *Jom* 68 (1) (2016) 170–177.
- [103] N. Limodin, L. Salvo, E. Boller, M. Suéry, M. Felberbaum, S. Gaillière, K. Madi, In situ and real-time 3-d microtomography investigation of dendritic solidification in an al-10 wt.% cu alloy, *Acta Materialia* 57 (7) (2009) 2300–2310.
- [104] B. Cai, J. Wang, A. Kao, K. Pericleous, A. Phillion, R. Atwood, P. Lee, 4d synchrotron x-ray tomographic quantification of the transition from cellular to dendrite growth during directional solidification, *Acta Materialia* 117 (2016) 160–169.
- [105] D. Tournet, J. Mertens, E. Lieberman, S. Imhoff, J. Gibbs, K. Henderson, K. Fezzaa, A. Deriy, T. Sun, R. Lebensohn, et al., From solidification processing to microstructure to mechanical properties: A multi-scale x-ray study of an al-cu alloy sample, *Metallurgical and Materials Transactions A* 48 (11) (2017) 5529–5546.
- [106] J. Gibbs, K. A. Mohan, E. Gulsoy, A. Shahani, X. Xiao, C. Bouman, M. De Graef, P. Voorhees, The three-dimensional morphology of growing dendrites, *Scientific reports* 5 (1) (2015) 1–9.
- [107] K. L. Elder, T. Stan, Y. Sun, X. Xiao, P. W. Voorhees, Microstructural characterization of dendritic evolution using two-point statistics, *Scripta Materialia* 182 (2020) 81–85.
- [108] D. Tournet, T. Isensee, L. Sturz, A. Viardin, M. Založnik, Comparing mesoscopic models for dendritic growth, conference MCWASP XV, Stockholm, Sweden (virtual conference), June 2020 (2020).
- [109] D. Tournet, A. J. Clarke, S. D. Imhoff, P. J. Gibbs, J. W. Gibbs, A. Karma, Three-dimensional multiscale modeling of dendritic spacing selection during Al-Si directional solidification, *JOM* 67 (8) (2015) 1776–1785.
- [110] J. Strickland, B. Nenchev, S. Perry, K. Tassenberg, S. Gill, C. Panwisawas, H. Dong, N. D’Souza, S. Irwin, On the nature of hexagonality within the solidification structure of single crystal alloys: Mechanisms and applications, *Acta Materialia* 200 (2020) 417–431.
- [111] N. Bergeon, D. Tournet, L. Chen, J.-M. Debierre, R. Guérin, A. Ramirez, B. Billia, A. Karma, R. Trivedi, Spatiotemporal dynamics of oscillatory cellular patterns in three-dimensional directional solidification, *Physical review letters* 110 (22) (2013) 226102.
- [112] Y. Song, S. Akamatsu, S. Bottin-Rousseau, A. Karma, Propagative selection of tilted array patterns in directional solidification, *Physical Review Materials* 2 (5) (2018) 053403.
- [113] N. Warnken, R. C. Reed, On the characterization of directionally solidified dendritic microstructures, *Metallurgical and Materials Transactions A* 42 (6) (2011) 1675–1683.
- [114] M. A. Tschopp, J. D. Miller, A. L. Oppedal, K. N. Solanki, Characterizing the local primary dendrite arm spacing in directionally solidified dendritic microstructures, *Metallurgical and Materials Transactions A* 45 (1) (2014) 426–437.
- [115] T. Takaki, S. Sakane, M. Ohno, Y. Shibuta, T. Shimokawabe, T. Aoki, Primary arm array during directional solidification of a single-crystal binary alloy: large-scale phase-field study, *Acta Materialia* 118 (2016) 230–243.
- [116] S. Liu, E. Martínez, J. LLorca, Prediction of the Al-rich part of the Al-Cu phase diagram using cluster expansion and statistical mechanics, *Acta Materialia* 195 (2020) 317–326.
- [117] S. Liu, G. Esteban-Manzanares, J. LLorca, First-principles analysis of precipitation in Mg-Zn alloys, *Physical Review Materials* 4 (2020) 093609.
- [118] J. J. Hoyt, M. Asta, A. Karma, Atomistic and continuum modeling of dendritic solidification, *Materials Science and Engineering: R: Reports* 41 (6) (2003) 121–163.
- [119] N. T. Brown, E. Martinez, J. Qu, Interfacial free energy and stiffness of aluminum during rapid solidification, *Acta Materialia* 129 (2017) 83–90.
- [120] H. Liu, B. Bellón, J. LLorca, Multiscale modelling of the morphology and spatial distribution of θ' precipitates in al-cu alloys, *Acta Materialia* 132 (2017) 611–626.
- [121] H. Liu, I. Papadimitriou, F. Lin, J. LLorca, Precipitation during high temperature aging of al-cu alloys: A multiscale analysis based on first principles calculations, *Acta Materialia* 167 (2019) 121–135.